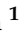# Thermodynamic Analysis of a Half-Effect Absorption Cooling System Powered by a Low-Enthalpy Geothermal Source

Javier Alejandro Hernández-Magallanes [1], Jonathan Ibarra-Bahena [2], Wilfrido Rivera [2], Rosenberg J. Romero [3], Efraín Gómez-Arias [4,*], Ulises Dehesa-Carrasco [5], Orlando Miguel Espinoza-Ojeda [6] and Sanal Kozhiparambil Chandran [1]

[1] Facultad de Ciencias Químicas, Universidad Autónoma de Nuevo León, Av. Universidad s/n, Ciudad Universitaria, San Nicolás de los Garza, Nuevo León 66455, Mexico; jahem@ier.unam.mx (J.A.H.-M.); skc@ier.unam.mx (S.K.C.)

[2] Instituto de Energías Renovables, Universidad Nacional Autónoma de México, Privada Xochicalco S/N, Col. Centro, Temixco, Morelos 62580, Mexico; jibarra@ier.unam.mx (J.I.-B.); wrgf@ier.unam.mx (W.R.)

[3] Centro de Investigación en Ingeniería y Ciencias Aplicadas, Universidad Autónoma del Estado de Morelos, Av. Universidad 1001, Col. Chamilpa, Cuernavaca, Morelos 62209, Mexico; rosenberg@uaem.mx

[4] CONACYT-Centro de Investigación Científica y de Educación Superior de Ensenada, División de Ciencias de la Tierra, Carretera Ensenada-Tijuana No. 3918, Zona Playitas, Baja California 22860, Mexico

[5] CONACYT-Instituto Mexicano de Tecnología del Agua, Paseo Cuauhnáhuac, 8532, Col. Progreso, Jiutepec, Morelos 62550, Mexico; udehesaca@conacyt.mx

[6] CONACYT-Instituto de Investigaciones en Ciencias de la Tierra, Universidad Michoacana de San Nicolás de Hidalgo, Edif. "U" Ciudad Universitaria, Morelia, Michoacán 58060, Mexico; omespinozaoj@conacyt.mx

* Correspondence: gomezar@cicese.mx; Tel.: +52-(646)-175-0500 (ext. 26085)

check for updates

Abstract: A thermodynamic analysis of a half-effect absorption cooling system powered by a low-enthalpy geothermal source was carried out. This paper presents modeling of the half-effect absorption cooling system operating with an ammonia/lithium nitrate mixture and based on the first and second laws of thermodynamics, using as energy inputs real data from two geothermal wells located at Las Tres Vírgenes volcanic complex, Baja California Sur, México. Plots of coefficients of performance and exergy efficiency against condenser, evaporator, and generator temperatures are presented for the half-effect cooling system. The results showed that the system was able to operate at generation temperatures between 56 and 70 °C, which were supplied by the geothermal wells in order to produce cooling at temperatures as low as −16 °C, achieving coefficients of performance between 0.10 and 0.36, while the exergy efficiency varied from 0.15 to 0.40 depending on the system operating temperatures.

Keywords: half-effect absorption system; geothermal source; low enthalpy; thermodynamic analysis

1. Introduction

Conventional vapor-compression cooling systems require large amounts of electrical energy to operate: This promotes energy consumption based on fossil fuels [1]. In recent years, research and technology development have been focused on efficient energy use as well as renewable energy sources to mitigate environmental problems (such as global warming or air, water, and soil pollution) and other related energy issues [2]. Among renewable energies, geothermal energy is considered to be an abundant and constant source of thermal energy, unlike thermal solar energy [3]. Geothermal resources of a high temperature are generally being utilized for electricity production, and the

installed capacity is continuously growing [4]. However, despite the vast potential of low-to-medium temperature geothermal resources, they are not being used because there are technical limitations to electricity generation (by low-temperature heat), low energy conversion efficiency, and high investment and production costs [5,6]. However, there is considerable potential for geothermal energy at a low-to-medium temperature (<150 °C): According to Stefansson [7], there is a potential for 1410 EJ/year. Air conditioning absorption systems are some of the most interesting devices, since they use low-to-medium temperature heat sources [8]. Air conditioning absorption systems operate with environmentally clean working fluids and require lower electricity consumption than conventional systems, so CO_2 emissions are very low [9]. Absorption systems can be used for large-scale applications, their cost is lower with respect to other thermally driven systems, they consume a negligible amount of electrical energy, and they have few mechanical parts [10]: This is an environmentally friendly method in order to produce air conditioning. However, a combination of renewable thermal energy and an absorption chiller mainly depends on the coupling temperature [11]. A single-effect absorption cooling system consists of a generator (G), an absorber (A), a condenser (C), an evaporator (E), and a heat exchanger (SHE), as can be seen in Figure 1. Heat is supplied to the generator to separate part of the refrigerant from the working mixture. The refrigerant goes to the condenser and then to the evaporator through the expansion valve. The refrigerant is evaporated, producing a cooling effect, and then goes to the absorber, where it is absorbed by the solution coming from the generator. The diluted solution is pumped to the generator, starting the cycle again.
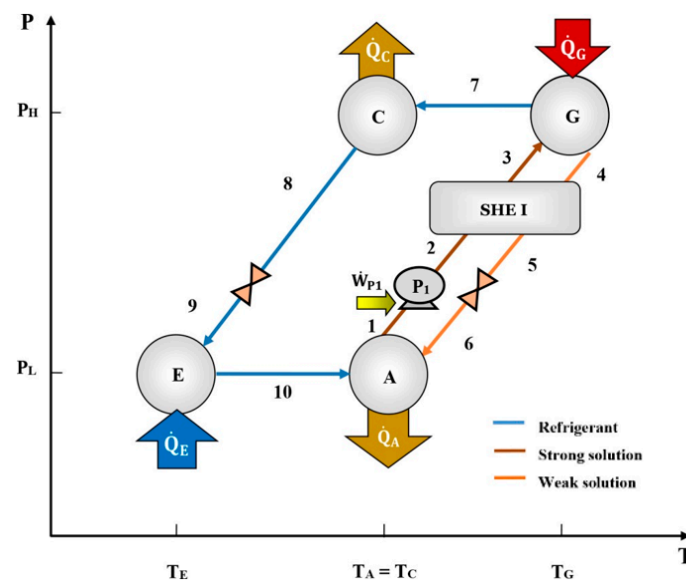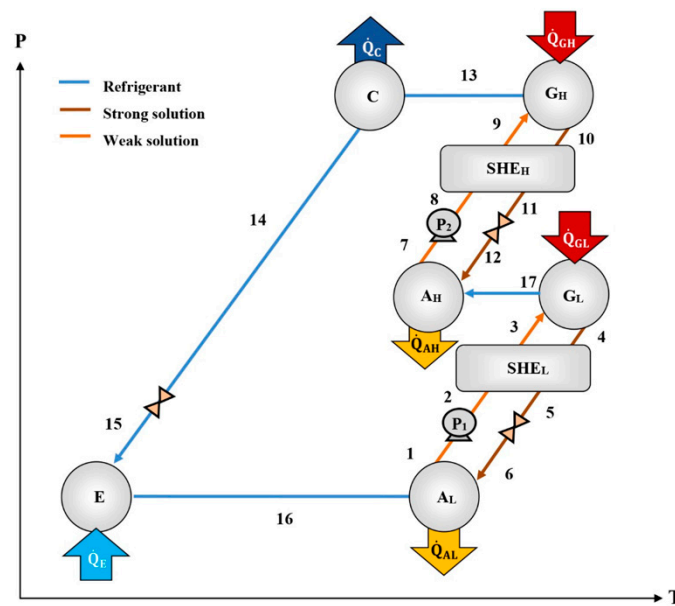

Figure 1. Pressure–Temperature diagram for a single-effect absorption cooling system.

Compared to the single-effect cycle, the half-effect cycle has two solution circuits, one of them at high pressure and the other one at low pressure, as can be seen in Figure 2 [12]. The heat is supplied to both generators (G_{HP} and G_{LP}) at the same temperature. The refrigerant fluid produced by the first solution circuit (in G_{LP}) is absorbed in the second solution circuit (in A_{HP}). Meanwhile, the refrigerant fluid vapor produced in the high-pressure generator (G_{HP}) is condensed, expanded, and evaporated to produce a cooling effect. The refrigerant fluid leaving the evaporator goes to the low-pressure absorber (A_{LP}), where it is absorbed by the solution coming from G_{LP}. The new strong solution is pumped to G_L, starting the cycle again. The half-effect cycle, despite having relatively low values of the coefficient of performance (COP) compared to the simple effect cycle [12,13], has the peculiarity that it can operate at extreme operating conditions, such as high condensing temperatures and low generation temperatures.

Figure 2. Pressure–Temperature diagram for a half-effect absorption cooling system.

In the literature, there have been many reports about theoretical and experimental works on single- and double-effect absorption systems: However, the literature about absorption half-effect systems is scarce. Cozzolino [14] described a residential micro-Combined Cooling, Heating and Power (CCHP) system, including a low-temperature Proton Exchange Membrane Fuel Cell (PEMFC) power unit and a half-effect lithium bromide absorption chiller. The author carried out numerical simulations in order to demonstrate the energetic feasibility and performance of this configuration. According to the author's results, the highest exergy utilization factor (ExUF) value was obtained for the minimum evaporator temperature (4 °C), minimum condenser temperature (27 °C), and 67 °C in both generators (high- and low-temperature) of the absorption chiller. Maryami and Dehghan [13] carried out a comparative theoretical analysis of five configurations of LiBr/water absorption refrigeration systems, included the half-effect configuration. Based on the authors' results, when the evaporator temperature was 4 °C with condenser temperatures of 33 °C and 39 °C, the half-effect system could be operated at lower generator temperatures, around 57 °C and 67 °C, respectively. The COP values calculated were approximately 0.40 and 0.42, respectively. This was a significant result because it meant that it was possible to use a heat source at a low thermal level that could be obtained from low-cost solar collectors or waste heat in order to produce air conditioning. Domínguez-Inzunza et al. [12] analyzed, through mathematical simulations, the performance of five different configurations of absorption cooling systems operating with ammonia/lithium nitrate. The authors concluded that the half-effect system might reach evaporator temperatures around 0 °C at generator temperatures as low as 50 °C, with a COP value around 0.3. Gebreslassie et al. [15] carried out an exergy analysis for single-, double-, triple-, and half-effect water/lithium bromide absorption cycles. According to the results, the highest exergy destruction rates in the cycle occurred on the two absorbers, followed by the two generators. As the heat source temperature increased, the concentration differences between incoming and leaving solutions in the generators and absorbers increased, which was accompanied by higher exergy destruction rates. Gomri [16] carried out a comparative study between single-effect and half-effect absorption cycles with an identical cold output and water/LiBr as a working mixture. The author demonstrated that the calculated COP of the half-effect system was approximately half of the COP of the single-effect system, but the exergy efficiency of the latter was slightly lower. The results of the thermodynamic analysis showed that, when the evaporation temperature was maintained at 4 °C, condenser and absorber temperatures varied from 28 °C to 38 °C; generator temperature varied from 40 °C to 80 °C; the maximum COP values for half-effect cooling systems were from

0.408 to 0.435; and the maximum exergy efficiency was from 14.7% to 22.6%. Besides, the author concluded that for generator temperatures higher than 78 °C, a single-effect system must be used, but on the other hand, when generator temperatures are less than 78 °C, it is recommended to use a half-effect system. Arivazhagan et al. [17] described a 1-kW cooling capacity half-effect absorption prototype, which used hydro chlorofluorocarbon (HFC)-based working fluids (R134a as refrigerant and N,N-dimethylacetamide (DMAC) as absorbent). According to the experimental performance evaluation, the evaporator temperature was as low as 7 °C, with generator temperatures from 55 to 75 °C. The optimum generator temperature was in the range of 65–70 °C, for which the coefficient of performance was 0.36.

According to the literature review, half-effect absorption systems show great potential in using low-temperature heat sources. In the present paper, thermodynamic and numerical heat transfer analyses are presented in order to demonstrate the feasibility of a half-effect absorption system driven by a low-enthalpy geothermal source. Two cases were analyzed: The first of them was used as an extreme case due to its low thermal level (<65 °C), and the second was considered a medium-temperature level heat source (>70 °C).

2. Proposed System

This paper proposes a half-effect absorption system powered by a geothermal resource for air conditioning and refrigeration applications, as shown in Figure 3. The proposed system uses NH_3-$LiNO_3$ as a working mixture and a low-enthalpy geothermal energy source to heat water up to 55 °C. In this case, a U-tube heat exchanger was used for the heat transfer process. Finally, this heated working fluid was used as a thermal energy source for the absorption refrigeration system.
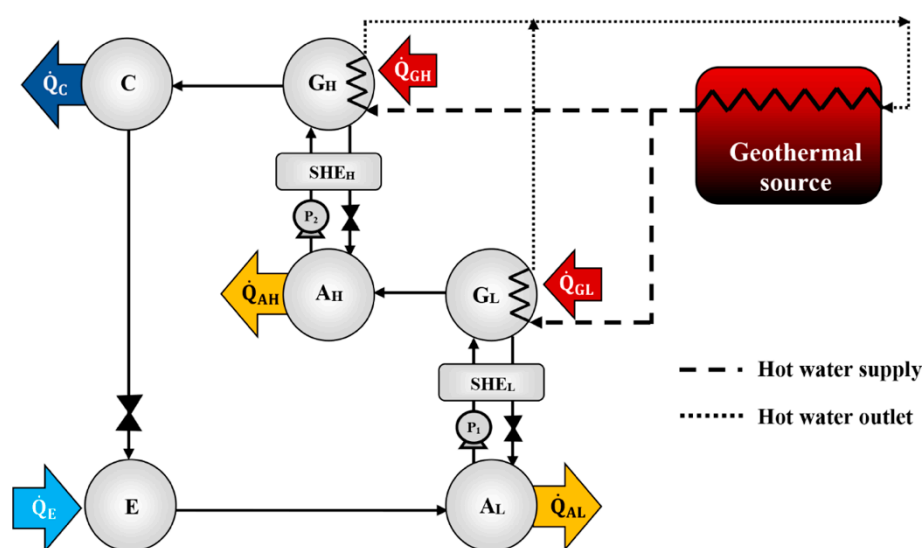

Figure 3. Schematic diagram of the interconnection between the geothermal resource and the half-effect cycle.

3. Methodology

### 3.1. Geothermal Source Modeling

In La Reforma caldera located at Las Tres Vírgenes volcanic complex, Baja California Sur, México (Figure 4), two shallow wells have been drilled in the last two years. The geothermal field Las Tres Vírgenes is located in this volcanic area. Currently, in this place, there is continuing geothermal exploration to evaluate and estimate geothermal potential for the generation of electrical energy and the feasibility of direct uses.
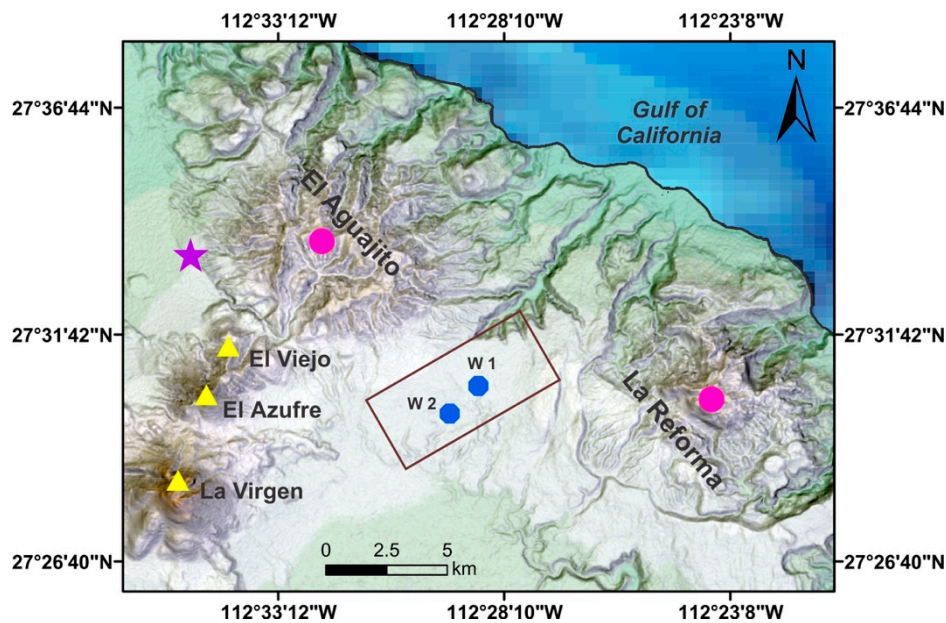
Figure 4. Location of shallow wells drilled (W1 and W2) in La Reforma caldera. The symbology corresponds as follows: Pink-filled circles for La Reforma and El Aguajito calderas, yellow-filled triangles for La Vírgen, El Azufre, and El Viejo volcanoes, and the purple star for a thermal spring called Agua-Agria.

For the present study, W1 (Figures 4 and 5) was used as a low-enthalpy geothermal energy source for heating water up to 55 °C in a U-tube heat exchanger (HE). This well had a depth of 50 m, with purely conductive thermal behavior (Figure 5).
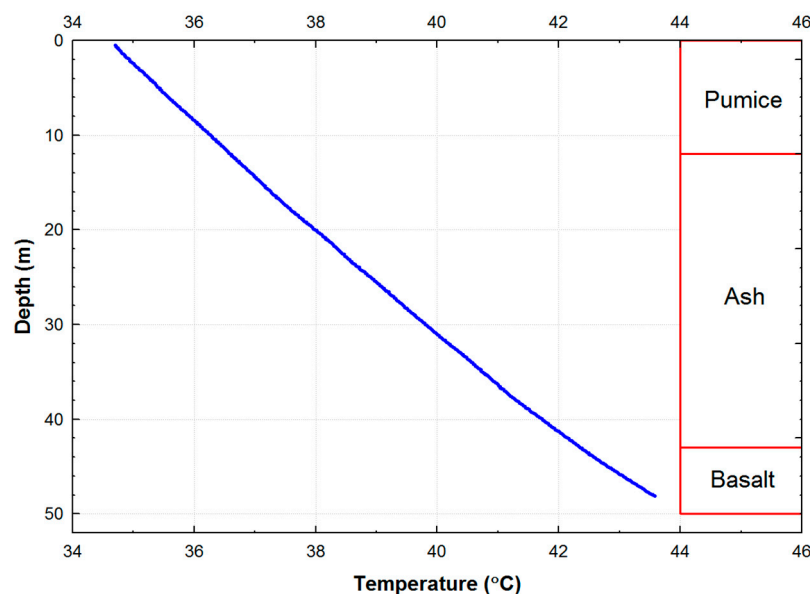
Figure 5. Temperature profile of well W1 (the maximum temperature was 43.5 °C to a depth of 48.0 m), including a lithology profile (right side).

For an estimation of the natural geothermal gradient, the bottom-hole temperature (*BHT*) versus time measurements to different depths was registered after a borehole drilling operation [18,19], and the Horner-plot method (Equation (1)) was used to estimate the static formation temperature (SFT)

to a 50-m depth. This method suggests a linear relationship between *BHT* measurements and the dimensionless Horner time that corresponds to the logarithmic function of the following equation:

$$BHT\,(\Delta t) = T_{HM} - b_{HM}\left[\ln\left(\frac{\Delta t + tc}{\Delta t}\right)\right],\tag{1}$$

where Δt and tc are the shut-in times after the cessation of drilling mud circulation (in hours) and the circulation time of the drilling fluid (in hours). The slope (b_{HM}) and intercept (T_{HM}) values can be estimated by a linear regression computation, and the T_{HM} value corresponds to the SFT.

3.2. Variation in Ground Temperature and Heat Transfer Process

The variation in ground temperature is caused by seasonal fluctuations of air temperature on the surface that can reach depths of around 20 m [20,21]. Equation (2) is used to describe the transient heat transfer in a semi-infinite solid, where T is temperature (°C), t is time (s), α is the thermal diffusivity (m^2/s), and Z is depth (m):

$$\frac{\partial T}{\partial t} = \alpha \frac{\partial^2 T}{\partial Z^2},\tag{2}$$

The shallow thermal perturbation behaves like a sinusoidal wave with time, and, for solving Equation (2), a sinusoidal temperature mathematical model is used [21,22]:

$$T(Z,t) = T_m + A_z \sin\left[\frac{2\pi}{P}(t - t_0) - \gamma Z\right] + \frac{\partial T}{\partial Z},\tag{3}$$

where $T(Z,t)$ is the ground temperature at time t (h) and depth Z (m); T_m is average surface temperature (°C); A_z is the amplitude of the ground annual surface temperature wave (obtained from Equation (4)); t_0 is the time lag needed (day of the year) for the ground surface temperature to reach the T_m value; and $\partial T/\partial Z$ is the geothermal gradient of 0.43 °C/m, which was calculated between the average of T_m = 25 °C ($Z = 0$) and SFT = 46.6 °C to Z = 50 m depth. Equations (4) and (5) was used to estimate the A_z value:

$$A_z = A_0 exp^{-\gamma z},\tag{4}$$

$$\gamma = \sqrt{\frac{\pi}{\alpha P}},\tag{5}$$

where γ is the inverse of the damping depth, and P is the period of the oscillation (365 days) in hours.

For the numerical heat transfer analysis between well W1 and the U-tube heat exchanger, the convective heat transfer process was evaluated, so for an estimation of the maximum water temperature to the heat exchanger outlet, the following empirical relationship for pipe and tube flow was used [21,23]:

$$\dot{Q} = h\pi dL\left(T_W - \frac{T_1 + T_2}{2}\right) = \dot{m}C_P(T_2 - T_1),\tag{6}$$

where h is the convective heat transfer coefficient (W/m^2 °C), d is the tube diameter (m), L is the total length of the well (m), T_W is the wall temperature along the depth of the tube, $\dot{m}$ is the mass flow (kg/s), Cp is the fluid heat capacity (J/kg °C), and T_1 and T_2 are the inlet and outlet system temperatures. In this study, T_2 corresponds to T_{max} or the heating temperature of water at depth. The turbulent flow in the inner part of U-tube was calculated using the empirical relation by Dittus and Boelter [23,24]:

$$Nu_d = 0.023\,Re_d^{0.8}\,Pr^n,\tag{7}$$

where Re_d and Pr correspond to Reynolds and Prandtl numbers, respectively, and the exponent n is equal to 0.4 for heating and 0.3 for cooling [24]. The thermal properties of water for temperatures between 20 and 100 °C were calculated from the following polynomial regression equations [21]:

$$k = 0.5576 + 0.0021T - 0.0296 \times 10^{-4}T^2 + 6.1869 \times 10^{-8}T^3, \tag{8}$$

$$\mu = 0.0018 - 5.805210 \times 10^{-5}T + 1.145710 \times 10^{-6}T^2 - 1.220410 \times 10^{-8}T^3 + 5.183910 \times 10^{-11}T^4, \tag{9}$$

$$\rho = 999.8556 + 0.0366T - 0.0064T^2 + 0.00002T^3, \tag{10}$$

$$C_P = 4225.9949 - 5.2960T + 0.2410T^2 - 0.0055T^3 + 6.2127 \times 10^{-5}T^4 - 2.6538\mathrm{x}10^{-7}T^5. \tag{11}$$

3.3. Simulation of Half-Effect Absorption Cooling System

For the analysis of the performance of the half-effect cycle, mathematical models were developed based on the first law of thermodynamics and the thermodynamic properties of the working mixture. The physical and thermodynamic properties of NH_3-$LiNO_3$ were obtained from Hernández-Magallanes et al. [25]. Meanwhile, the properties of pure NH_3 were provided by Tillner-Roth [26] and Infante Ferreira [27]. The assumptions for the modeling of the thermodynamic cycle were the following:

I.   The system operates in thermodynamic equilibrium;
II.   The analysis is made under steady-state conditions;
III.   The solution is in a saturated state when leaving generators and absorbers;
IV.   The refrigerant is in a saturated state when leaving the condenser and evaporator;
V.   Heat losses and pressure drops in the tubing and the components are considered negligible;
VI.   Flow through the valves is isenthalpic.

In addition, isentropic efficiencies of 0.8 and 0.7 were considered for the pumps and the solution heat exchangers, respectively, [28] and the heat supplied to both generators was at the same temperature, $T_{G\_HP} = T_{G\_LP}$. Steady-state mass and energy balances for the components of the half-effect cycle were established as follows:

Low-Pressure Generator (G_{LP})

$$\dot{m}_3 = \dot{m}_4 + \dot{m}_{17}, \tag{12}$$

$$\dot{m}_3 X_3 = \dot{m}_4 X_4 + \dot{m}_{17} X_{17}, \tag{13}$$

$$\dot{Q}_{G\_LP} = \dot{m}_4 H_4 + \dot{m}_{17} H_{17} - \dot{m}_3 H_3, \tag{14}$$

Low-Pressure Absorber (A_{LP})

$$\dot{m}_1 = \dot{m}_6 + \dot{m}_{16}, \tag{15}$$

$$\dot{m}_1 X_1 = \dot{m}_6 X_6 + \dot{m}_{16} X_{16}, \tag{16}$$

$$\dot{Q}_{A\_LP} = \dot{m}_6 H_6 + \dot{m}_{16} H_{16} - \dot{m}_1 H_1, \tag{17}$$

High-Pressure Generator (G_{HP})

$$\dot{m}_9 = \dot{m}_{10} + \dot{m}_{13}, \tag{18}$$

$$\dot{m}_9 X_9 = \dot{m}_{10} X_{10} + \dot{m}_{13} X_{13}, \tag{19}$$

$$\dot{Q}_{G\_HP} = \dot{m}_{10} H_{10} + \dot{m}_{13} H_{13} - \dot{m}_9 H_9, \tag{20}$$

High-Pressure Absorber (A_{HP})

$$\dot{m}_7 = \dot{m}_{12} + \dot{m}_{17}, \tag{21}$$

$$\dot{m}_7 X_7 = \dot{m}_{12} X_{12} + \dot{m}_{17} X_{17}, \tag{22}$$

$$\dot{Q}_{A\_HP} = \dot{m}_{12} H_{12} + \dot{m}_{17} H_{17} - \dot{m}_7 H_7, \tag{23}$$

Condenser (C)

$$\dot{Q}_C = \dot{m}_{13}(H_{13} - H_{14}), \tag{24}$$

Evaporator (E)

$$\dot{Q}_E = \dot{m}_{15}(H_{16} - H_{15}), \tag{25}$$

Efficiency of the Solution Heat Exchanger at Low Pressure (SHE$_{LP}$)

$$\eta_{SHE\_LP} = \frac{H_3 - H_2}{H_4 - H_2}, \tag{26}$$

Efficiency of the Solution Heat Exchanger at High Pressure (SHE$_{HP}$)

$$\eta_{SHE\_HP} = \frac{H_9 - H_8}{H_{10} - H_8}, \tag{27}$$

Pump Work at Low Pressure $\left(\dot{W}_{LP} \right)$

$$\dot{W}_{LP} = \dot{m}_1(H_2 - H_1), \tag{28}$$

Pump Work at High Pressure $\left(\dot{W}_{HP} \right)$

$$\dot{W}_{HP} = \dot{m}_7(H_8 - H_7), \tag{29}$$

Medium Pressure System (P$_M$)

$$P_M = PF * P_H, \tag{30}$$

Coefficient of Performance (COP)

$$COP = \frac{\dot{Q}_E}{\dot{Q}_{G\_LP} + \dot{Q}_{G\_HP} + \dot{W}_{LP} + \dot{W}_{HP}}, \tag{31}$$

Exergy Efficiency (η_{EX})

$$\eta_{EX} = \frac{\left(\frac{T_0^* - T_E^*}{T_E^*} \right) \dot{Q}_E}{\dot{Q}_{G\_LP}\left(1 - \frac{T_0^*}{T_{G\_LP}^*} \right) + \dot{Q}_{G\_HP}\left(1 - \frac{T_0^*}{T_{G\_HP}^*} \right) + \dot{W}_{LP} + \dot{W}_{HP}}, \tag{32}$$

Irreversibility $\left(\dot{I} \right)$

$$\dot{I} = \dot{Ex}_{supply} - \dot{Ex}_{useful}, \tag{33}$$

$$\dot{I} = \left[\dot{Q}_{G\_LP}\left(1 - \frac{T_0^*}{T_{G\_LP}^*} \right) + \dot{Q}_{G\_HP}\left(1 - \frac{T_0^*}{T_{G\_HP}^*} \right) + \dot{W}_{LP} + \dot{W}_{HP} \right] - \left[\dot{Q}_E\left(\frac{T_0^* - T_E^*}{T_E^*} \right) \right], \tag{34}$$

4. Results and Discussion

4.1. Simulation of the Geothermal Source

4.1.1. Analysis of Ground Temperature Variation

From the Santa Rosalía meteorological station, we obtained the daily surface air temperature data for the year 2017 to calculate the parameters from Equation (3). The ground temperature variation from depth $Z = 0$ to $Z = 100$ m was calculated considering the daily temperature means to be $T_m = 28.35$ °C and $A_0 = 8.31$ °C. The parameter γ (m−1) was estimated using the thermophysical properties of the rocks from W1 (Table 1), the period $P = 8760$ h (365 days), and $t_0 = 1728$ h (this value corresponded

to the 72nd day of the year). Substituting all of these into Equation (3), the thermal ground variation from La Reforma caldera was estimated by the following equation:

$$T(Z,t) = 28.35 + 8.31 exp^{-\gamma Z} \sin \left[\frac{2\pi}{8760} (t - 1728) - \gamma Z \right] + 0.43 \, °C/m, \tag{35}$$

Figure 6 shows the thermal profile of the ground temperature for depths between 0 and 100 m for each month of the year. We found that the seasonal thermal effect reached depths between 15 and 18 m, and that the simulated temperature for $Z = 50$ m (depth of drilled W1) corresponded to $T = 48.6 \, °C$ and $Z = 100$ m to $T = 68.6 \, °C$.

Table 1. Thermophysical properties of the drilled cores from W1 [29].

Rock	Density (kg/m^3)	Heat Capacity (J/kg·°C)	Thermal Conductivity (W/m·°C)
Pumice (0–12 m)	2360	885	1.768
Ash (12–43 m)	2180	920	1.535
Basalt (43–50 m)	2700	880	2.200
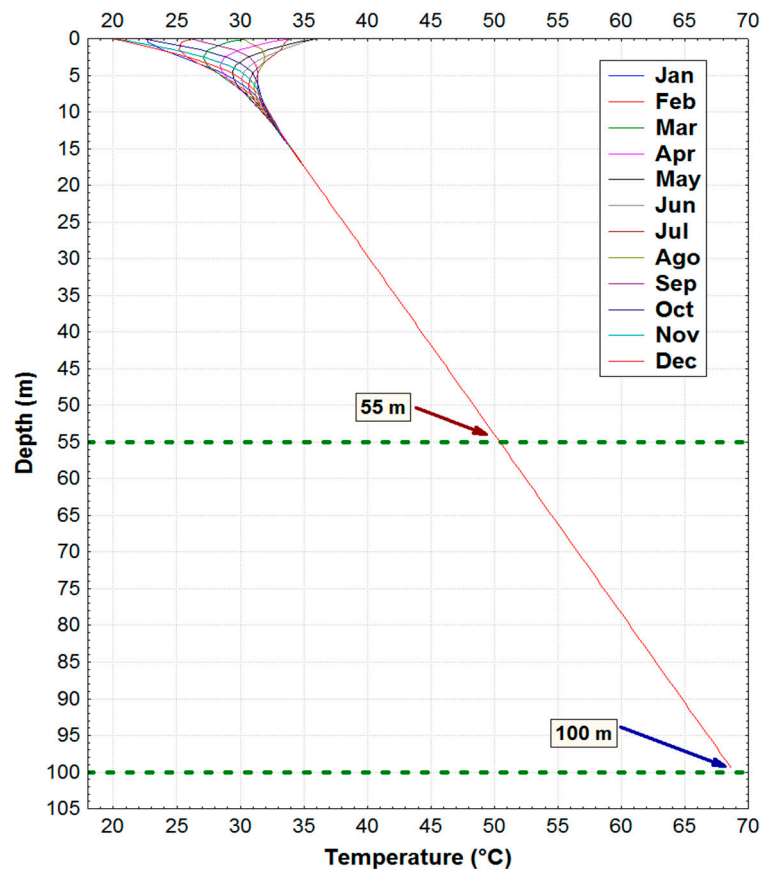
Figure 6. Thermal profile of the ground temperature variation for 100 m of depth for each month of the year 2017 (from La Reforma caldera).

4.1.2. Analysis of Heat Transfer on a U-Tube Heat Exchanger

Case 1

The first case corresponded to the numerical heat transfer between W1 and the U-tube heat exchanger for an estimation of the maximum water heating temperature in the heat exchanger. The initial parameters used for this analysis were $d = 0.0254$ m [29], $L = 100$ m [29], and fluid velocity $v =$

1 m/s (to the inlet and outlet of the heat exchanger). The thermal properties of water corresponding to k, ρ, μ, and Cp were calculated using Equations (8)–(11). Under these conditions, 12 heat transfer models were simulated in the U-tube heat exchanger (the thermal ground profile obtained for each month corresponded to T_W), and for all models, the values of T_{max} were located between 88 and 100 m of depth with temperatures from 65.0 °C to 67.6 °C (Figure 7). If we assumed that the U-tube could be isolated from a depth of 91 m to the surface (only in the ascending section of the fluid) and assumed that the heat losses were negligible, the heat load Q (kW) from the system achieved a value of 2.029 kW (Figure 7). From these results, it was clear that it was possible to use the well W1 as a low-enthalpy geothermal energy source coupled to a half-effect absorption system for air conditioning and refrigeration applications.
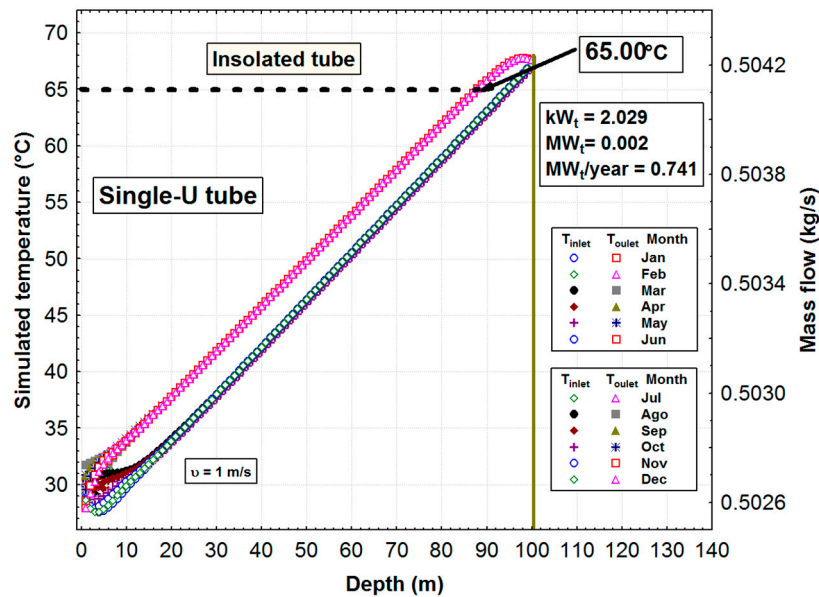

Figure 7. Temperatures simulated along the U-tube heat exchanger in well W1.

Case 2

The second case was a thermal analysis of well W-LV5 from Las Tres Vírgenes geothermal field (an inoperative well): The Comisión Federal de Electricidad (CFE) uses it only as a monitoring well. W-LV5 had a depth of 1800 m, and the static formation temperature at different depths has been reported by Verma et al. [30]. Figure 8 shows the temperature profile of W-LV5, which had purely conductive thermal behavior. The maximum temperature reported was 219.3 °C to a depth of 1800 m.

For the numerical heat transfer between W-LV5 and the U-tube heat exchanger for the estimation of the maximum water heating temperature in the heat exchanger, we considered the diameter of the U-tube to be 0.0254 m, the total length to be 1850 m, and fluid velocity to be $\upsilon = 7$ m/s. The thermal properties of water (k, ρ, μ, and Cp) for interval temperatures between 20 °C and 300 °C were calculated using the polynomial regression in Equations (36)–(38) (these equations were obtained from thermodynamics data values of water to high temperatures). A geothermal gradient of 156.7 °C/km was estimated from the SFTs of W-LV5 as showed in Figure 8. The heat transfer model result in the U-tube heat exchanger is shown in Figure 9, where T_{max} at the exit was 72.8 °C. Theoretically, with this result, it was also possible to use well W-LV5 as a low-enthalpy source coupled to the half-effect absorption systems to produce cooling:
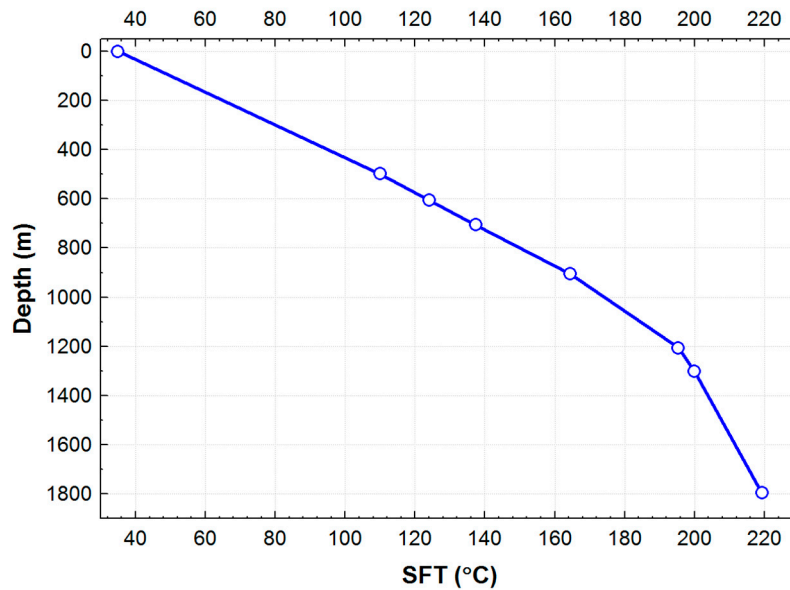
$$k = 0.5561 + 0.0024T - 1.2930 \times 10^{-5}T^2 + 8.7655 \times 10^{-9}T^3 + 1.0073 \times 10^{-10}T^4 - 2.5537 \times 10^{-13}T^5, \quad (36)$$

$$u = 0.0017 - 4.4804 \times 10^{-5}T + 5.5960 \times 10^{-7}T^2 - 3.4932 \times 10^{-9}T^3 + 1.0418 \times 10^{-11}T^4 - 1.179410^{-14}T^5, \quad (37)$$
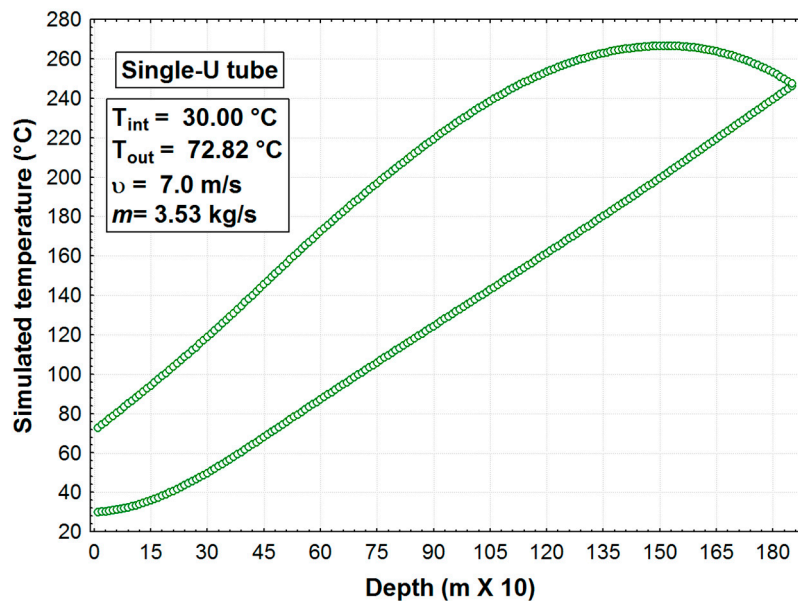
$$\rho = 1002.2885 - 0.1898T - 0.0024T^2 - 6.8357 \times 10^{-7}T^3, \tag{38}$$

$$C_P = 4165.2926 + 7.4586T - 0.2692T^2 + 0.0032T^3 - 1.4370 \times 10^{-5}T^4 + 2.2723 \times 10^{-8}T^5. \tag{39}$$

Figure 8. Temperature profile from static formation temperatures of well W-LV5 from Las Tres Vírgenes geothermal field (reported by Verma et al. [30]).

Figure 9. Temperature simulated along the U-tube heat exchanger in well W-LV5. T_{out} corresponds to the temperature of water to the heat exchanger outlet, υ to fluid velocity, and m to mass flow.

4.2. Simulation of Half-Effect Absorption Cooling System

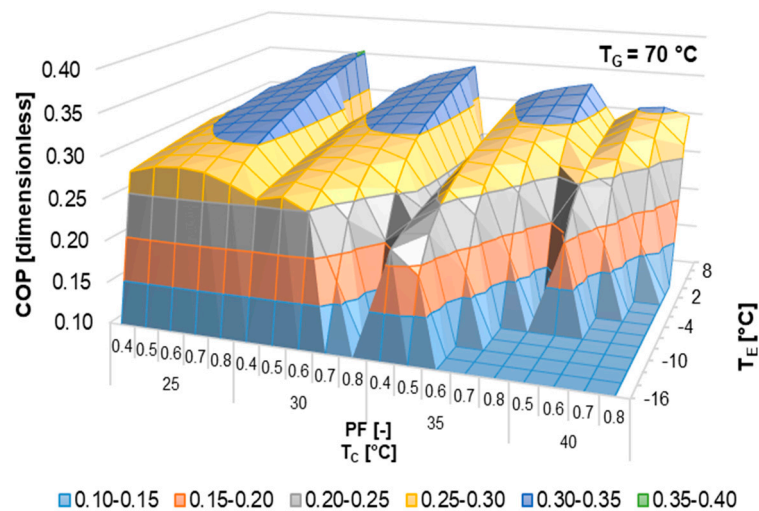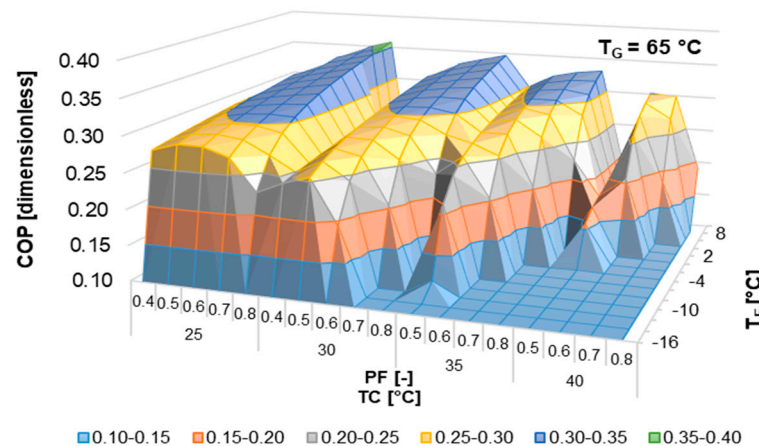#### 4.2.1. Analysis of COP of the Half-Effect Cycle

The simulation of the half-effect cycle was performed considering the temperatures of both geothermal wells described previously.

Table 2 shows the operating ranges of the main variables involved in the thermodynamic analysis.

**Table 2.** Operation range of selected variables for the half-effect cycle.

Variable	Range
Condensation temperature, (T_C)	25 to 40 °C
Evaporation temperature, (T_E)	−16 to 10 °C
Generation temperature, (T_G)	56 to 70 °C
Pressure factor, (PF)	0.4 to 0.8

The present section shows a sensitivity analysis of the operation of the half-effect cycle for the different operating conditions. In Figures 10–13, the COP of the system is shown as a function of the evaporation temperature (T_E) and the pressure factor (PF) for different condensing temperatures (T_C), keeping fixed the thermal source or generation temperature (T_G).

Figure 10. Coefficient of performance (COP) of the half-effect cycle against PF and T_E for different T_C. Analyzed case: T_G = 70 °C.

Figure 11. COP of the half-effect cycle against PF and T_E for different T_C. Analyzed case: T_G = 65 °C.
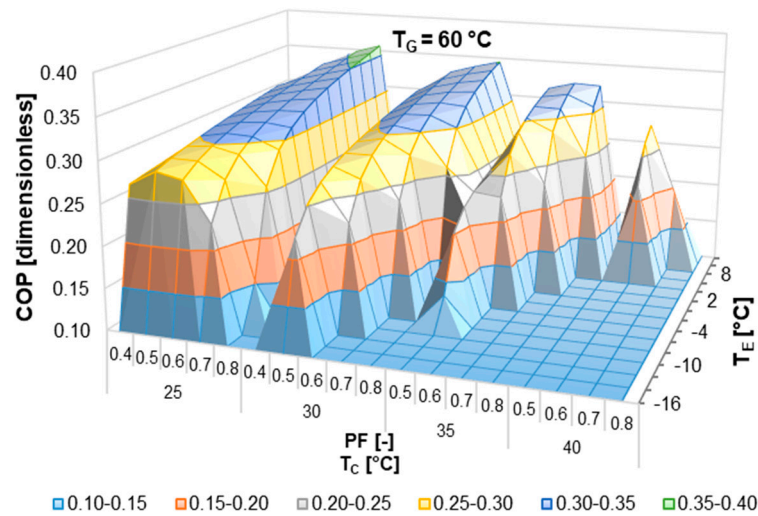
Figure 12. COP of the half-effect cycle against *PF* and T_E for different T_C. Analyzed case: T_G = 60 °C.
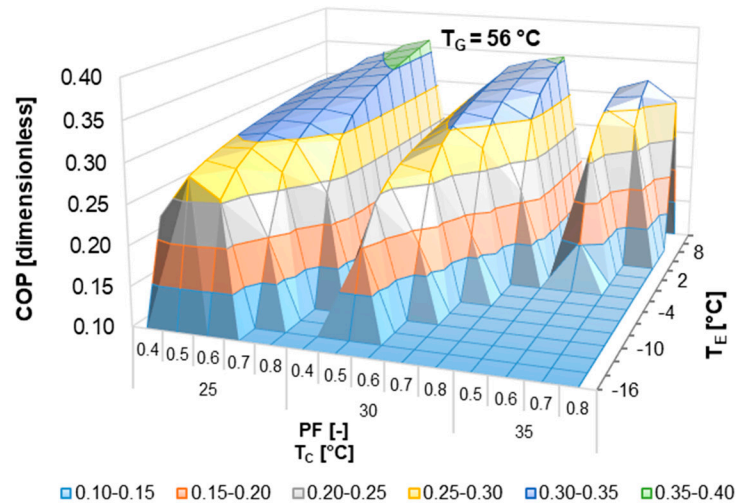
Figure 13. COP of the half-effect cycle against *PF* and T_E for different T_C. Analyzed case: T_G = 56 °C.

Figures 10–13 show the variation of the COP as a function of the condensation temperature (T_C), the pressure factor (*PF*), and the evaporation temperature (T_E) of the half-effect cycle for different values of the generation temperature (T_G). In all the figures, it can be seen that the COP was directly proportional to the evaporation temperature and inversely proportional to the condensation temperature. Besides, for a fixed condensing temperature, better COPs were obtained for high pressure factors (*PF*): However, at high *PF* values, low evaporation temperatures could not be achieved. Therefore, depending on the particular application of the system (cooling or air conditioning) the *PF* value was set. The *PF* defined the mean pressure of the cycle, and this factor was fixed through the concentration of the working mixture.

From Figure 10, it can be seen that the coefficients of performance varied from 0.10 to 0.36 at T_G = 70 °C. It can be observed that for condenser temperatures of 25, 30, and 35 °C, the half-effect cycle could work for refrigeration and freezing since it could achieve evaporation temperatures as low as −16 °C with coefficients of performance between 0.25 and 0.36. However, at T_C = 40 °C (only at PF values of 0.5 and 0.6), the system was still capable of being used for refrigeration, but at higher PF values the system could only be used for food conservation or air conditioning.

Figure 11 shows COP variations from 0.10 to 0.36 at a generation temperature of 65 °C. Evaporation temperatures of −16, −16, −12, and −4 °C could be reached at condensation temperatures of 25, 30,

35, and 40 °C, respectively, for low values of *PF*. As the condenser temperature increased, the cycle significantly reduced its ability to operate as a cooling system. Thus, from this plot, it is clear that the system reduced its capability of producing cooling with increments in the condensation temperature. This happened because at higher condensation temperatures, the pressure of the system increased, raising the boiling point of the mixture and thus reducing the amount of the refrigerant produced. Nevertheless, it is important to mention that even at high condensation temperatures, the system could still be used for food conservation or air conditioning.

In Figure 12, it can be seen that the coefficients of performance were very similar to reported in Figure 11. However, due to the generation temperature being lower (T_G = 60 °C), it was more difficult to achieve lower evaporation temperatures with this system. For example, at a condensation temperature of 35 °C, evaporation temperatures of −10, −4, 0, and 4 °C were obtained for *PFs* of 0.5, 0.6, 0.7, and 0.8, respectively. These evaporation temperatures were slightly lower than those reported in Figure 10. For a *PF* of 0.5 and 0.6, the system could operate for refrigeration, while for *PF* values of 0.7 and 0.8 the system could operate only for air conditioning.

Finally, Figure 13 shows the variation of the coefficients of performance as a function of the condensation and evaporation temperatures at a generation temperature of 56 °C. As was expected, further reducing the thermal source reduced the operating conditions of the half-effect cycle. This was mainly due to the crystallization range of the working mixture, which restricted the operation of the thermodynamic cycle [31]. For these conditions, it was no longer possible to operate the thermodynamic cycle at condensation temperatures above 35 °C.

4.2.2. Analysis of η_{Ex} of the Half-Effect Cycle

Figures 14 and 15 show the analysis of the exergy efficiency for the operating conditions established in Table 2.
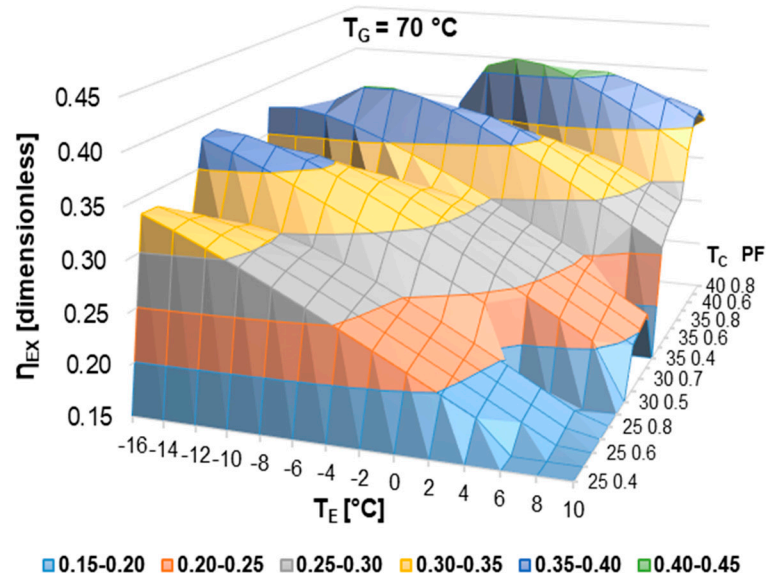
Figure 14. Exergy efficiency (η_{Ex}) against T_E and *PF* for different T_C. Analyzed case: T_G = 70 °C.

Figure 14 shows the exergy efficiency as a function of the evaporator and condenser temperatures at a generation temperature of 70 °C. From the exergy efficiency (Equation (32)), it can be seen that the η_{EX} values were directly proportional to the cooling effect and also that they increased at lower evaporation temperatures. This happened because at lower evaporator temperatures, the difference between T_0 and T_E increased, thus increasing exergy efficiency. For these conditions, the exergy efficiencies varied from 0.15 to 0.40.
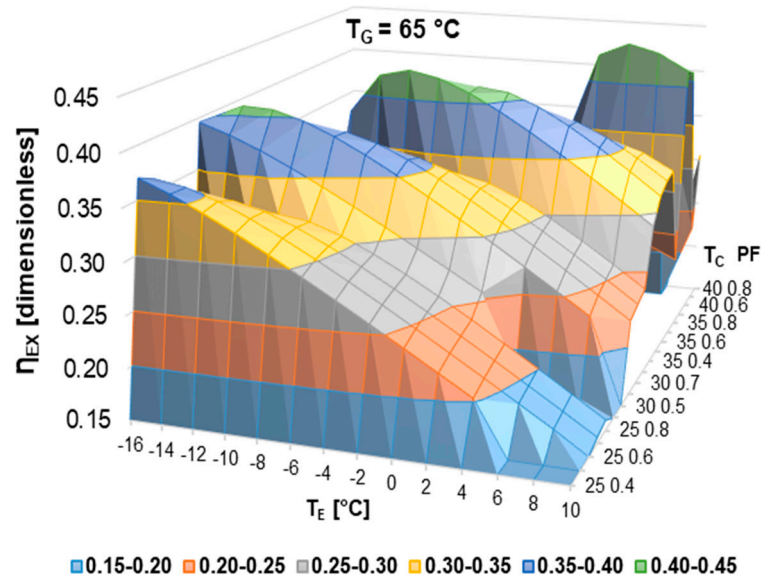
Figure 15. Exergy efficiency (η_{Ex}) against T_E and PF for different T_C. Analyzed case: $T_G = 65\ ^\circ$C.

Figure 15 shows the exergy efficiency again as a function of the condenser and evaporation temperature, but now at a generation temperature of 65 °C. In this figure, a similar trend for exergy efficiency is observed, as shown in Figure 14. Comparing both figures, it can be seen that the exergy values were slightly higher in Figure 15 at a generation temperature of 65 °C than those reported in Figure 14 at 70 °C. This was expected, since it is known that at higher temperature differences, higher irreversibilities occur in the system, causing a decrease in exergy efficiency. In addition, in both figures, it can be seen that the cycle operating range decreased at higher values of T_C and PF in a way similar to what is shown in Figures 10–13, for the reasons explained in those figures.

4.3. Study Cases: Geothermal Wells 1 and LV5

The results obtained from the modeling of half-effect cooling systems operating with heat supplied from two real geothermal wells is presented in this section. According to Figure 7, theoretically, well W1 has the capability of transferring heat (<65 °C) to secondary fluid (water), which would be used to supply energy to the generator of the half-effect cooling system. Tables 3 and 4 present the results of the modeling for refrigeration ($T_E = -6\ ^\circ$C) and air conditioning ($T_E = 10\ ^\circ$C), respectively.

As can be seen from Table 3, the system was capable of operating for refrigeration at generation temperatures of 56 and 64 °C with condenser temperatures of 25 and 30 °C. The system produced up to 1.05 Kw of cooling at $T_E = -6\ ^\circ$C, with a coefficient of performance around 0.3. On the other hand, the system was capable of producing air conditioning at the same generation temperatures, but with condenser temperatures of 25, 30, 35, and 40 °C. The highest value of the cooling capacity obtained was 1.19 Kw, with a coefficient of performance of 0.36.

On the other hand, according to Figure 9, W-LV5 had the capability to transfer heat to a stream of water at temperatures up to 70 °C, with a mass flow rate of 3.53 kg/s. Tables 5 and 6 summarize the results of the modeling of the coupled system at the same temperatures from Tables 3 and 4 for refrigeration and air conditioning, respectively.

Table 3. Performance summary of the modeling of well W1 coupled to a half-effect cooling system. Case study: Refrigeration ($T_E = -6$, $PF = 0.7$).

T_C (°C)	25		30
T_G (°C)	56	64	64
Thermal Power (kW)			
Cooling Capacity ($\dot{Q}_E$)	1.04	1.05	0.93
Condenser heat duty ($\dot{Q}_C$)	1.14	1.17	1.03
Low-pressure absorber heat output ($\dot{Q}_{A\_LP}$)	1.78	1.71	1.89
Low-pressure generator heat input ($\dot{Q}_{G\_LP}$)	1.89	1.85	1.99
High-pressure absorber heat output ($\dot{Q}_{A\_HP}$)	1.45	1.49	1.33
High-pressure generator heat input ($\dot{Q}_{G\_HP}$)	1.44	1.48	1.32
Mechanical Power (kW)			
Solution pump 1 ($\dot{W}_{LP}$)	5.5×10^{-3}	3.3×10^{-3}	1.1×10^{-2}
Solution pump 2 ($\dot{W}_{HP}$)	8.9×10^{-4}	7.7×10^{-4}	9.2×10^{-4}
Performance Indicator			
Coefficient of performance, COP (-)	0.31	0.31	0.28
Exergy efficiency, η_{Ex} (-)	0.38	0.32	0.37
Irreversibility, $\dot{I}$ (kW)	0.44	0.51	0.47

Table 4. Performance summary of the modeling of well W1 coupled to a half-effect cooling system. Case study: Air conditioning ($T_E = 10$, $PF = 0.7$).

T_C (°C)	25		30		35		40
T_G (°C)	56	64	56	64	56	64	64
Thermal Power (kW)							
Cooling Capacity ($\dot{Q}_E$)	1.19	1.16	1.16	1.13	1.10	1.09	0.98
Condenser heat duty ($\dot{Q}_C$)	1.29	1.28	1.24	1.23	1.17	1.19	1.06
Low-pressure absorber heat output ($\dot{Q}_{A\_LP}$)	1.60	1.58	1.64	1.62	1.72	1.68	1.83
Low-pressure generator heat input ($\dot{Q}_{G\_LP}$)	1.71	1.71	1.75	1.74	1.81	1.79	1.92
High-pressure absorber heat output ($\dot{Q}_{A\_HP}$)	1.63	1.63	1.60	1.59	1.53	1.56	1.42
High-pressure generator heat input ($\dot{Q}_{G\_HP}$)	1.62	1.61	1.58	1.58	1.51	1.54	1.40
Mechanical Power (kW)							
Solution pump 1 ($\dot{W}_{LP}$)	3.1×10^{-4}	3.0×10^{-4}	1.3×10^{-3}	9.7×10^{-4}	5.0×10^{-3}	2.8×10^{-3}	1.2×10^{-2}
Solution pump 2 ($\dot{W}_{HP}$)	1.0×10^{-3}	8.5×10^{-4}	1.4×10^{-3}	1.1×10^{-3}	2.1×10^{-3}	1.5×10^{-3}	2.0×10^{-3}
Performance Indicators							
Coefficient of performance, COP (-)	0.36	0.35	0.35	0.34	0.33	0.33	0.29
Exergy efficiency, η_{Ex} (-)	0.20	0.16	0.31	0.24	0.46	0.34	0.44
Irreversibility, $\dot{I}$ (Kw)	0.38	0.45	0.35	0.42	0.32	0.39	0.35

Table 5. Performance summary of the modeling of well W-LV5 coupled to a half-effect cooling system. Case study: Refrigeration ($T_E = -6$, $PF = 0.7$).

T_C (°C)	25		30		35
T_G (°C)	65	70	65	70	70
Thermal Power (kW)					
Cooling capacity ($\dot{Q}_E$)	22.00	21.80	19.80	20.40	12.40
Condenser heat duty ($\dot{Q}_C$)	24.66	24.70	22.11	23.04	13.95
Low-pressure absorber heat output ($\dot{Q}_{A\_LP}$)	35.99	35.50	39.28	37.58	50.62
Low-pressure generator heat input ($\dot{Q}_{G\_LP}$)	38.85	38.58	41.67	40.36	51.64
High-pressure absorber heat output ($\dot{Q}_{A\_HP}$)	31.48	31.61	28.62	29.90	18.38
High-pressure generator heat input ($\dot{Q}_{G\_HP}$)	31.20	31.35	28.32	29.61	18.17
Mechanical Power (kW)					
Solution pump 1 ($\dot{W}_{LP}$)	0.07	0.06	0.20	0.13	0.72
Solution pump 2 ($\dot{W}_{HP}$)	0.02	0.02	0.02	0.02	0.01
Performance Indicator					
Coefficient of performance, COP (-)	0.31	0.31	0.28	0.29	0.18
Exergy efficiency, η_{Ex} (-)	0.31	0.28	0.37	0.34	0.26
Irreversibility, $\dot{I}$ (kW)	10.92	11.77	10.13	11.06	9.76

Table 6. Performance summary of the modeling of well W-LV5 coupled to a half-effect cooling system. Case study: Air conditioning ($T_E = 10$, $PF = 0.7$).

T_C (°C)	25		30		35		40		45
T_G (°C)	65	70	65	70	65	70	65	70	70
Thermal Power (kW)									
Cooling capacity ($\dot{Q}_E$)	24.40	24.05	23.70	23.35	22.90	22.60	20.95	21.40	7.60
Condenser heat duty ($\dot{Q}_C$)	26.90	26.79	26.02	25.92	25.01	24.98	22.75	23.53	8.30
Low-pressure absorber heat output ($\dot{Q}_{A\_LP}$)	33.19	32.92	34.09	33.81	35.19	34.78	37.99	36.48	59.52
Low-pressure generator heat input ($\dot{Q}_{G\_LP}$)	35.97	35.92	36.72	36.66	37.63	37.46	39.99	38.87	58.80
High-pressure absorber heat output ($\dot{Q}_{A\_HP}$)	34.33	34.29	33.67	33.64	32.87	32.92	30.42	31.53	11.35
High-pressure generator heat input ($\dot{Q}_{G\_HP}$)	34.03	34.01	33.32	33.32	32.46	32.54	29.97	31.10	11.17
Mechanical Power (kW)									
Solution pump 1 ($\dot{W}_{LP}$)	0.01	0.01	0.02	0.02	0.06	0.05	0.21	0.13	1.58
Solution pump 2 ($\dot{W}_{HP}$)	0.02	0.02	0.02	0.02	0.03	0.03	0.04	0.03	0.02
Performance Indicator									
Coefficient of performance, COP (-)	0.35	0.34	0.34	0.33	0.33	0.32	0.30	0.31	0.11
Exergy efficiency, η_{Ex} (-)	0.16	0.14	0.23	0.20	0.32	0.28	0.43	0.37	0.18
Irreversibility, $\dot{I}$ (kW)	9.60	10.47	8.97	9.85	8.33	9.21	7.64	8.55	7.64

From Table 5, it is possible to see that the half-effect cooling system was capable of operating at generation temperatures of 65 and 70 °C at condenser temperatures of 25, 30, and 35 °C. For this case, the cooling system was able to provide up to 22 kW of refrigeration at $T_E = -6$ °C with a coefficient of performance of 0.31.

From Table 6, it can be observed that the system could provide up to 24.4 kW of cooling for air conditioning ($T_E = 10$ °C), achieving a coefficient of performance of 0.35.

Comparing the results obtained from well W1 to well W-LV5, it was clear that the cooling capacity obtained from the absorption cooling system was directly related to the power of each well. Tables 4 and 5 show that even for a geothermal well with low power, it was still possible to produce a cooling effect, and of course if the temperatures and power of the geothermal well were higher, as in the case of well W-LV5, the cooling capacity increased considerably.

5. Conclusions

A thermodynamic analysis of a half-effect absorption cooling system powered by a low-enthalpy geothermal source was carried out. For the modeling, real data of two geothermal wells located in México were used. One of the geothermal wells (W1) was used as an extreme case due to its low thermal temperature and power capacity, and the other (W-LV5) was used as the most realistic heat source. The results showed that even for the extreme case, the half-effect absorption cooling system was able to operate, but obtained a low cooling effect. Meanwhile, by using the second geothermal well (W-LV5), the cooling system was able to produce up to 22 kW of cooling capacity at an evaporator temperature of −6 °C, and up to 24.4 kW of cooling capacity at an evaporator temperature of 10 °C. In both cases, the coefficients of performance varied between 0.10 and 0.36, while the exergy efficiency varied from 0.15 to 0.40 depending on the system operating temperatures.

Nomenclature

1, 2, 3 . . .	Thermodynamic state points
A	Absorber
BHT	Bottom-hole temperature (°C)
C	Condenser
C_P	Heat capacity (J/kg °C)
COP	Coefficient of performance (dimensionless)
d	Diameter (m)
E	Evaporator
$\dot{Ex}$	Exergy (kW)
G	Generator

H	Specific enthalpy (kJ/kg)
h	Convective heat transfer coefficient (W/m^2 $^\circ$C)
$\dot{I}$	Irreversibility (kW)
k	Thermal conductivity (W/m$\cdot^\circ$C)
L	Length (m)
$\dot{m}$	Mass flow rate (kg/s)
P	Pressure (kPa)
P	Period (h)
PF	Pressure factor
$\dot{Q}$	Thermal capacity (kW)
SHE	Solution heat exchanger
T	Temperature ($^\circ$C)
T^*	Absolute temperature (K)
t	Time (s, h)
$\dot{W}$	Mechanical power (kW)
X	Concentration of the solution (% weight/weight)
Z	Depth (m)
Subscripts	
0	Thermodynamic environment
A	Absorber
C	Condenser
E	Evaporator
Ex	Exergy
G	Generator
HP	High pressure
LP	Low pressure
M	Medium pressure
P	Pump
M	Average temperature ($^\circ$C)
W	Wall
Greek letters	
η	Efficiency (-)
ν	Specific volume (m^3/kg)
α	Thermal diffusivity (m^2/s)
γ	Inverse of damping (1/m)
μ	Viscosity (kg/m$\cdot$s)
ρ	Density (kg/m^3)

References

1. Santamouris, M.; Argiriou, A. Renewable energies and energy conservation technologies for buildings in southern Europe. *Int. J. Sol. Energy* **1994**, *15*, 69–79. [CrossRef]
2. Panwar, N.L.; Kaushik, S.C.; Kothari, S. Role of renewable energy sources in environmental protection: A review. *Renew. Sustain. Energy Rev.* **2011**, *15*, 1513–1524. [CrossRef]
3. Pastor-Martinez, E.; Rubio-Maya, C.; Ambriz-Díaz, V.M.; Belman-Flores, J.M.; Pacheco-Ibarra, J.J. Energetic and exergy performance comparison of different polygeneration arrangements utilizing geothermal energy in cascade. *Energy Convers. Manag.* **2018**, *168*, 252–269. [CrossRef]
4. Bertani, R. Geothermal power generation in the world 2010–2014 update report. *Geothermics* **2016**, *60*, 31–43. [CrossRef]
5. Astolfi, M.; Romano, M.C.; Bombarda, P.; Macchi, E. Binary ORC (organic Rankine cycles) power plants for the exploitation of medium-low-temperature geothermal sources–Part A: Thermodynamic optimization. *Energy* **2014**, *66*, 423–434. [CrossRef]
6. Walraven, D.; Laenen, B.; D'haeseleer, W. Comparison of thermodynamic cycles for power production from low-temperature geothermal heat sources. *Energy Convers. Manag.* **2013**, *66*, 220–233. [CrossRef]

7. Stefánsson, V. Estimate of the world geothermal potential. In Proceedings of the 20th Anniversary Workshop of the United Nations University, Geothermal Training Program, Reykjavik, Iceland, 13–14 October 1998; pp. 111–120.

8. Wang, J.; Zheng, D. Performance of one and a half-effect absorption cooling cycle of H2O/LiBr system. *Energy Convers. Manag.* **2009**, *50*, 3087–3095. [CrossRef]

9. Chua, K.J.; Chou, S.K.; Yang, W.M. Advances in heat pump systems: A review. *Appl. Energy* **2010**, *87*, 3611–3624. [CrossRef]

10. Leonzio, G. Solar systems integrated with absorption heat pumps and thermal energy storages: State of art. *Renew. Sustain. Energy Rev.* **2017**, *70*, 492–505. [CrossRef]

11. Xu, Z.Y.; Wang, R.Z. Solar-powered absorption cooling systems. In *Advances in Solar Heating and Cooling*; Wang, R.Z., Ge, T.S., Eds.; Woodhead Publishing: Cambridge, UK, 2016; pp. 251–298, ISBN 978-0-08-100301-5.

12. Domínguez-Inzunza, L.A.; Hernández-Magallanes, J.A.; Sandoval-Reyes, M.; Rivera, W. Comparison of the performance of single-effect, half-effect, double-effect in series and inverse and triple-effect absorption cooling systems operating with the NH3-LiNO3 mixture. *Appl. Therm. Eng.* **2014**, *66*, 612–620. [CrossRef]

13. Maryami, R.; Dehghan, A.A. An exergy based comparative study between LiBr/water absorption refrigeration systems from half effect to triple effect. *Appl. Therm. Eng.* **2017**, *124*, 103–123. [CrossRef]

14. Cozzolino, R. Thermodynamic performance assessment of a novel micro-CCHP system based on a low-temperature PEMFC power unit and a half-effect Li/Br absorption chiller. *Energies* **2018**, *11*, 315. [CrossRef]

15. Gebreslassie, B.H.; Medrano, M.; Boer, D. Exergy analysis of multi-effect water–LiBr absorption systems: From half to triple effect. *Renew. Energy* **2010**, *35*, 1773–1782. [CrossRef]

16. Gomri, R. Performance analysis of low hot source temperature absorption cooling systems. *Int. J. Ambient Energy* **2010**, *31*, 143–152. [CrossRef]

17. Arivazhagan, S.; Saravanan, R.; Renganarayanan, S. Experimental studies on HFC based two-stage half effect vapor absorption cooling system. *Appl. Therm. Eng.* **2006**, *26*, 1455–1462. [CrossRef]

18. Espinoza-Ojeda, O.M.; Santoyo, E.; Andaverde, J. A new look at the statistical assessment of approximate and rigorous methods for the estimation of stabilized formation temperatures in geothermal and petroleum wells. *J. Geophys. Eng.* **2011**, *8*, 233–258. [CrossRef]

19. Liu, C.; Li, K.; Chen, Y.; Jia, L.; Ma, D. Static formation temperature prediction based on bottom hole temperature. *Energies* **2016**, *9*, 646. [CrossRef]

20. Jensen-Page, L.; Narsilio, G.A.; Bidarmaghz, A.; Johnston, I.W. Investigation of the effect of seasonal variation in ground temperature on thermal response tests. *Renew. Energy* **2018**, *125*, 609–619. [CrossRef]

21. Galindo-Luna, Y.R.; Gómez-Arias, E.; Rosenberg, J.; Venegas-Reyes, E.; Montiel-González, M.; Unland-Weiss, H.E.K.; Pacheco-Hernández, P.; González-Fernández, A.; Díaz-Salgado, J. Hybrid solar-geothermal energy absorption air-conditioning system operating with NaOH-H$_2$O–Las Tres Vírgenes (Baja California Sur), "La Reforma" case. *Energies* **2018**, *11*, 1268. [CrossRef]

22. Ozgener, O.; Ozgener, L.; Tester, J.W. A practical method to predict soil temperature variations for geothermal (ground) heat exchangers applications. *Int. J. Heat Mass Transf.* **2013**, *62*, 473–480. [CrossRef]

23. Holman, J.P. *Heat Transfer*, 6th ed.; McGraw-Hill Book Co.: Singapore, 1986.

24. Dittus, F.W.; Boelter, L.M.K. *Heat Transfer in Automobile Radiators of the Tubular Type*; University of California: Berkeley, CA, USA, 1930; Volume 2.

25. Hernández-Magallanes, J.A.; Rivera, W.; Coronas, A. Comparison of single and double stage absorption and resorption heat transformers operating with the ammonia-lithium nitrate mixture. *Appl. Therm. Eng.* **2017**, *125*, 53–68. [CrossRef]

26. Tillner-Roth, R.; Harms-Watzenberg, F.; Baehr, H.D. Eine neue fundamentalgleichung für ammoniak. *Dkv-tagungsbericht* **1993**, *20*, 167–181.

27. Ferreira, C.A.I. Thermodynamic and physical property data equations for ammonia-lithium nitrate and ammonia-sodium thiocyanate solutions. *Sol. Energy* **1984**, *32*, 231–236. [CrossRef]

28. Hernández-Magallanes, J.A.; Domínguez-Inzunza, L.A.; Gutiérrez-Urueta, G.; Soto, P.; Jiménez, C.; Rivera, W. Experimental assessment of an absorption cooling system operating with the ammonia/lithium nitrate mixture. *Energy* **2014**, *78*, 685–692. [CrossRef]

29. Sarbu, I.; Sebarchievici, C. General review of ground-source heat pump systems for heating and cooling of buildings. *Energy Build.* **2014**, *70*, 441–454. [CrossRef]

30. Verma, S.P.; Pandarinath, K.; Santoyo, E.; González-Patida, E.; Torres-Alvarado, I.; Tello-Hinojosa, E. Fluid chemistry and temperatures prior to exploitation at the Las Tres Vírgenes geothermal field, Mexico. *Geothermics* **2006**, *35*, 156–180. [CrossRef]

31. Hernández-Magallanes, J.A.; Heard, C.L.; Best, R.; Rivera, W. Modeling of a new absorption heat pump-transformer used to produce heat and power simultaneously. *Energy* **2018**, *165*, 112–133. [CrossRef]